Inactivation of the dimeric Rap$_{pLS20}$ anti-repressor of the conjugation operon is mediated by peptide-induced tetramerization

Isidro Crespo [1], **Nerea Bernardo**[1], **Andrés Miguel-Arribas**[2], **Praveen K. Singh**[2],
Juan R. Luque-Ortega[3], **Carlos Alfonso**[4], **Marc Malfois**[1], **Wilfried J.J. Meijer** [2,*] **and**
Dirk Roeland Boer [1,*]

[1]ALBA Synchrotron Light Source, C. de la Llum 2-26, Cerdanyola del Vallès, 08290 Barcelona, Spain, [2] Centro de Biología Molecular 'Severo Ochoa' (CSIC-UAM), C. Nicolás Cabrera 1, Universidad Autónoma, Canto Blanco, 28049 Madrid, Spain, [3]Molecular Interactions Facility, Centro de Investigaciones Biológicas Margarita Salas (CSIC), C. Ramiro de Maeztu 9, 28040 Madrid, Spain and [4]Systems Biochemistry of Bacterial Division Lab, Centro de Investigaciones Biológicas Margarita Salas (CSIC), C. Ramiro de Maeztu 9, 28040 Madrid, Spain

ABSTRACT

Quorum sensing allows bacterial cells to communicate through the release of soluble signaling molecules into the surrounding medium. It plays a pivotal role in controlling bacterial conjugation in Gram-positive cells, a process that has tremendous impact on health. Intracellular regulatory proteins of the RRNPP family are common targets of these signaling molecules. The RRNPP family of gene regulators bind signaling molecules at their C-terminal domain (CTD), but have highly divergent functionalities at their N-terminal effector domains (NTD). This divergence is also reflected in the functional states of the proteins, and is highly interesting from an evolutionary perspective. Rap$_{pLS20}$ is an RRNPP encoded on the *Bacillus subtilis* plasmid pLS20. It relieves the gene repression effectuated by Rco$_{pLS20}$ in the absence of the mature pLS20 signaling peptide Phr*$_{pLS20}$. We report here an in-depth structural study of apo and Phr*$_{pLS20}$-bound states of Rap$_{pLS20}$ at various levels of atomic detail. We show that apo-Rap$_{pLS20}$ is dimeric and that Phr*$_{pLS20}$-bound Rap forms NTD-mediated tetramers. In addition, we show that Rap$_{pLS20}$ binds Rco$_{pLS20}$ directly in the absence of Phr*$_{pLS20}$ and that addition of Phr*$_{pLS20}$ releases Rco$_{pLS20}$ from Rap$_{pLS20}$. This allows Rco$_{pLS20}$ to bind the promotor region of crucial conjugation genes blocking their expression.

INTRODUCTION

Quorum sensing in bacterial cells is a process that allows bacterial cells to exchange information about their state and content (1). The external signals are used by cells to change the expression profile of their genes thereby affecting many processes that are candidates for interference in some way, including the control of expression of virulence factors and the control of bacterial conjugation. In Gram-positive bacteria, the mechanism of action of the signaling molecules is either through activation of a kinase-dependent signaling cascade (the two-component pathway), or by direct interaction with a transcriptional regulator.

The RRNPP family of Gram-positive tetratricopeptide repeat (TPR) proteins (2,3) was so named after discovery of the main representatives of the family, i.e. the proteins Rgg, Rap, NprR, PrgX and PlcR (4–7). In Gram-positive bacteria, RRNPP proteins play a crucial role in quorum sensing (8,9), where they serve as targets of their cognate signaling polypeptide. This peptide is produced, secreted, processed and then reimported into the bacterial cells that also produce the RRNPP. The mature, processed signaling peptide generally consists of a small fragment of the C-terminus of the full-length pre-proprotein, generally about 5–10 amino acids in length (10). Binding of the processed peptide to the C-terminal TPR domain of RRNPP proteins modulates interaction between the RRNPP protein and an effector molecule, leading to further downstream effects. Interaction with effector molecules depends on the N-terminal domain (NTD; effector domain) of the RRNPP (6,11). Thus, the nature of the effector molecule and therefore the function of the RRNPP proteins depend on the type

of effector domain incorporated at the N-terminus. The RRNPP-mediated quorum sensing mechanism is involved in the regulation of a variety of bacterial processes including conjugation (e.g. PrgX from the enterococcal plasmid pCF10), sporulation (e.g. RapA from *Bacillus subtilis*) and pathogenicity (e.g. PlcR from *B. cereus*) (7,12), and is found in a range of human commensal or pathogenic Gram-positive bacterial genera such as *Bacillus*, *Streptococcus* and *Enterococcus* (13). Interestingly, RRNPP-like proteins have been found beyond the realm of Gram-positive bacterial genomes, as illustrated by the recent structure determination of a regulator of phage lysis-lysogeny, AimR (14), or in the NlpI protein from Gram-negative *Escherichia coli*, which contains a lipobox motif that anchors it to the membrane (15).

The effector domains of RRNPP proteins known to date can be classified into three groups. The effector domains of the DNA-binding RNPP subclass of proteins are helix-turn-helix (HTH) motifs that are able to negatively regulate protein expression by binding DNA, examples of which are the PrgX protein from *Enterococcus faecalis* and the PlcR protein from *Bacillus thuringiensis*. A second group of proteins, exemplified by *B. subtilis* RapA, RapB, RapE, RapH and RapJ, contains an NTD with phosphatase activity. These proteins form a link in a phosphorylation cascade that translates the peptide signal into a downstream effect. The third group, which includes RapC, RapF, RapG, RapH and RapK, blocks the action of their cognate effector protein by direct interaction, directly or indirectly modulating expression that alters differentiation pathways. Note that RapH belongs to both least two groups as it exhibits both activities. Similarly, NprR contains both a phosphatase and a HTH domain. The variety in functions of different types of RRNPP proteins is also reflected in the differences in oligomerization state and the effect that the peptide can have on oligomerization. Different Rap proteins, even within a single functional class, have been found as monomers, dimers and tetramers, and these oligomerization states may change or remain the same depending on the presence of the peptide. For example, RapJ and RapF are found as monomers (16,17), whereas RapH is reported to be a dimer in solution (18). It seems that the aggregation behavior of RRNPP proteins does not depend directly on the functionality of the NTD, and there is no obvious common theme in how the oligomerization state of the different RRNPP family members relates to the mechanism (19).

Bacillus subtilis encodes 11 Rap proteins on its chromosome (6,10,20), and at least five plasmid-encoded variants (21,22). A recently identified *B. subtilis* RRNPP member (22,23), Rap_{pLS20}, is encoded by the Gram-positive *B. subtilis* conjugative plasmid pLS20. It lacks the conserved residues essential for phosphatase activity and has been shown to regulate the conjugation process. The conjugation genes of pLS20 are located in a single large operon that is under the control of the conjugation promoter P_c. By default, this promoter is repressed by the pLS20-encoded transcriptional regulator Rco_{pLS20} (23). Rap_{pLS20} activates conjugation by acting as an antirepressor of Rco_{pLS20} (22), which induces the formation of a DNA loop by binding to two closely located recognition sequences near the P_c, thereby inhibiting expression of the conjugation genes and

plasmid transfer (23). Rap_{pLS20} is essential to activate transcription of the conjugation genes by releasing Rco_{pLS20}-mediated P_c repression, which may involve a direct interaction between both. The presence of the Phr^*_{pLS20} peptide antagonizes the antirepressive action of Rap_{pLS20}, reverting the system to its default state (22). The pre-proprotein Phr_{pLS20} is a 44-amino acid protein, and after secretion, it is subject to a second processing step resulting in the release of the C-terminal 5 amino acids (QKGMY), which can be reimported in an *opp*-dependent manner (22). The genetic switch constituted by the aforementioned components is tightly regulated due to its design. However, the structural basis underlying this mechanism has not been reported.

Here, we demonstrate that Rap_{pLS20} can interact directly with either Rco_{pLS20} or Phr^*_{pLS20}. In addition, we have determined the crystal structures of Rap_{pLS20} in the apo form as well as in the peptide-bound form to understand the structural mechanism behind peptide-mediated release of antirepression of Rco_{pLS20} by Rap_{pLS20}. The structures are validated by SAXS measurements in solution. Surprisingly, our work reveals a tetrameric oligomerization state of Rap_{pLS20} in the presence of the peptide mediated by the NTDs, which has not been observed for other Rap proteins. The oligomerization state and structural changes introduced by peptide binding are compared with information available for other RRNPP members. We find that the peptide-induced change in orientation of the NTDs observed for Rap_{pLS20} is different to that observed for other RRNPP proteins. Thus, the position of the NTDs in apo and peptide-bound forms depends very much on the associated functionality. Implications of the structural findings on the mechanism of action of Rap_{pLS20} are discussed.

MATERIALS AND METHODS

Sequence alignments

A set of Rap_{pLS20}-like protein sequences was retrieved using an iterative PSI-BLAST search for 11 iterations and standard parameters. The representation of the sequence homology was obtained using the HMM-LOGO program (24).

Protein expression and purification

Rap_{pLS20} and Rco_{pLS20} were expressed and purified using standard protocols. *Escherichia coli* BL21 (DE3) were transformed with pET-28b carrying the insert of rap_{pLS20} or rco_{pLS20} containing a C-terminal His-tag and were inoculated in fresh Luria-Bertani broth (LB) media complemented with 50 µg/ml kanamycin at 37°C overnight. Then, the cells from the overnight culture were collected by centrifugation (4000 × g for 30 min) and suspended in expression media (typically 0.5 l of terrific broth (TB) with 50 µg/ml kanamycin), at a ratio of 30 ml of preculture per liter of medium. Cells in expression media were grown at 37°C until an $OD_{600} = 0.8$–1 was reached. After that, protein expression was induced overnight at 20°C by addition of 1 mM isopropyl β-D-1-thiogalactopyranoside (IPTG, Omnipur).

After overnight induction, cells were centrifuged at 4000 × g for 30 min, and pellets were frozen and resus-

pended in lysis buffer at a ratio of 5 ml/g of cells. The lysis buffer used for Rap_{pLS20} contained 50 mM Tris–HCl pH 8.0, 250 mM NaCl, 1% (v/v) glycerol, 10 mM $MgCl_2$, 1 mM EDTA, 1 mM β-mercapto-ethanol, 1 mM PMSF, and the buffer used for Rco_{pLS20} contained 20 mM Tris–HCl pH 8.0, 500 mM NaCl, 1% (v/v) glycerol, 10 mM $MgCl_2$, 1 mM EDTA, 1 mM β-mercapto-ethanol, 1 mM PMSF. The cell suspension was lysed adding DNAseI to a a final concentration of 200 μg/ml and lysozyme to a final concentration of 100 μg/ml during sonication. Insoluble matter was precipitated by centrifugation (18 000 × g, 30 min), and supernatant was filtered through a 0.22-μm filter and applied to a nickel-charged His-Trap™ HP chelating column 5 ml (GE Healthcare Life Sciences). The column was washed with 10 column volumes of bind buffer (20 mM Tris–HCl pH 8.0, 500 mM NaCl, 5 mM Imidazole) to elute unspecific bound proteins. Bound proteins were eluted using a 5–100 mM imidazole gradient in 20 mM Tris–HCl pH 8.0, 500 mM NaCl. Fractions containing protein were concentrated with an Amicon ultra 10 kDa MWCO (Millipore) and the buffer was exchanged using a PD-10 desalting column (GE Healthcare life sciences) to 20 mM Tris–HCl pH 8.0, 250 mM NaCl, 10 mM $MgCl_2$, 1 mM EDTA, 1% (v/v) glycerol buffer for Rap_{pLS20} and to 500 mM NaCl, 20 mM Tris–HCl pH 8.0 buffer for Rco_{pLS20}. Typically, a yield of ∼100 mg of Rap_{pLS20} and ∼20 mg of Rco_{pLS20} were obtained from 10 g of pellet. Purity was assessed to be >95% by SDS–PAGE, followed by Coomassie Blue staining. Protein concentration was determined by nanodrop and was used for assays immediately where possible or stored in aliquots at -80°C.

Analytical size exclusion chromatography on Rap_{pLS20} and Rco_{pLS20} mixtures

To determine the elution volumes of the separate proteins, 25 μg (0.56 nmol) of Rap_{pLS20} and 25 μg (1.2 nmol) Rco_{pLS20}, respectively, were injected on a Superdex 200 increase 5/150 GL equilibrated with 500 mM NaCl, 20 mM TRIS pH 8, and eluted at a flow rate of 0.2 ml/min. The concentrations of Rap_{pLS20} and Rco_{pLS20} solutions were 1 mg/ml, or 22.5 μM and 49.4 μM, respectively. For complex binding stoichiometry tests, molar ratios of 1:2, 1:4, 1:1 and 2:1 (Rco_{pLS20}:Rap_{pLS20}) were prepared and incubated for 30 min on ice before injection. To study the effect of Phr^*_{pLS20} peptide on Rap_{pLS20}/Rco_{pLS20} complex formation, a 5:1 Phr^*_{pLS20}:Rap_{pLS20} stoichiometry was used; 25 μl were injected in all cases. All total protein concentrations were within a 0.75–1.25 mg/ml range. To estimate the molecular weights (M_w) of the homo- and heterocomplexes, a calibration of the Superdex 200 increase 5/150 GL column was performed using proteins with known M_w, which were eluted using the same elution buffer used above. The derived relation between the elution volume (V_{el}) and M_w was V_{el} = –0.6815 · log(M_w) + 5.1906, with an R^2 = 0.933.

Sedimentation velocity assays (SV)

Samples of protein Rap_{pLS20} in 20 mM Tris, 250 mM NaCl, 10 mM $MgCl_2$, 1 mM EDTA, 0.1 mM β-mercaptoethanol and 1% (v/v) glycerol, pH 7.4, were loaded (320 μl) into

12-mm Epon-charcoal standard double-sector centerpieces. The assays were performed at 48 000 rpm in an XL-I analytical ultracentrifuge (Beckman-Coulter Inc.) equipped with both UV–VIS absorbance and Raleigh interference detection systems, using an An-50Ti rotor. Sedimentation profiles were recorded simultaneously by Raleigh interference and absorbance at 280 nm. Differential sedimentation coefficient distributions were calculated by least-squares boundary modelling of sedimentation velocity data using the continuous distribution $c(s)$ Lamm equation model as implemented by SEDFIT (25). These experimental s values were corrected to standard conditions using the program SEDNTERP (26) to get the corresponding standard s values (s20,w). For apo Rap_{pLS20}, measurements were performed at 4.5 and 25 μM (0.2–1.1 mg/ml). For the Rap-Phr complex, a Rap_{pLS20} concentration of 4.5 μM (0.2 mg/ml) was used.

Sedimentation equilibrium assays (SE)

Short column (95 μl) SE experiments of Rap_{pLS20} were carried out at speeds ranging from 7000 to 10 000 rpm and at 280 nm, using the same experimental conditions and instrument as in the SV experiments. A last high-speed run (48 000 rpm) was done to deplete protein from the meniscus region to obtain the corresponding baseline offsets. Weight-average buoyant M_w of Rap_{pLS20}, alone or in the presence of the Phr^*_{pLS20} peptide, were obtained by fitting a single-species model to the experimental data using the HeteroAnalysis program (27), once corrected for temperature and solvent composition with the program SEDNTERP (26).

Fluorescence polarization binding assays

Binding of the Phr^*_{pLS20} peptide was assayed in a CLARIOstar plate reader (BMG Labtech) on an OptiPlate-384 Black well plate (PerkinElmer) in 10 μl final assay volume. The Phr^*_{pLS20} peptide (GQKGMY, the glycine residue was added at the N-terminus to avoid interference with the dye) used for fluorescence polarization measurements was synthesized with an N-terminal fluorescein label and purified by ThermoFischer Scientific. The buffer used for the fluorescence polarization assays was 20 mM Tris pH 7.5, 150 mM NaCl, 1 mM DTT and 0.01% (v/v) Triton X-100. All buffers were properly degassed under vacuum and oxygen was removed saturating with nitrogen to prevent methionine oxidation. The protein concentration was varied from 0.1–100 μM and the peptide concentration was 50 nM. An excitation wavelength of 485 nm and an emission wavelength of 528 nm were used. For equilibrium competition binding assays, different concentrations of native Phr^*_{pLS20} (QKGMY) ranging from 0.6–1250 μM were tested, with constant concentrations of Rap_{pLS20} (10 μM) and 6-FAM-Phr^*_{pLS20} (50 nM). The data was measured at 25°C and corrected for background by subtracting the free-labeled peptide background. All the data treatment was done as previously described (28) and the data was fitted to a hyperbolic function for a single binding site using Origin 2018 (OriginLab Corporation).

SAXS analysis

Different concentrations of Rap_{pLS20}, ranging from 0.5 to 5 mg/ml (11.3–113 μM), and Rco_{pLS20}, ranging from 1.44 to 14.4 mg/ml for Rco_{pLS20} (70.9–709 μM), were tested to ensure proper scattering and signal detection. In the case of $Rap_{pLS20}/Phr^*_{pLS20}$ samples, the same concentrations were tested in the presence of 5-fold peptide molar concentration. All the samples were prepared in a final buffer consisting of 15 mM HEPES pH 7.5, 150 mM NaCl, 1 mM DTT. SAXS data on Rap_{pLS20} and Phr^*_{pLS20} mixtures were collected at NCD-SWEET beamline (BL11, ALBA Synchrotron, Barcelona). The final buffer was collected for subtraction of Rap_{pLS20} samples, and the buffer plus the highest Phr^*_{pLS20} concentration was also collected to ensure that no observable scattering was produced by the Phr^*_{pLS20} peptide. Measurements were carried out at 293 K in a quartz capillary of 1.5 mm diameter and 0.01 mm wall thickness. The data (20 frames with an exposure time of 0.5 sec/frame) were recorded using a Pilatus 1M detector (Dectris, Switzerland) at a sample-detector distance of 2.56 m and a wavelength λ = 1.0 Å.

Data on mixtures of Rap_{pLS20}, Rco_{pLS20} and Phr^*_{pLS20} were measured on beamline BM29 at the ESRF, using the automatic sample changer. The concentration ranged from 0.5 to 5 mg/ml (11.3–113 μM) for Rap and 1.44 to 14.4 mg/ml for Rco (70.9–709 μM). Ten consecutive frames were collected with a photon-counting Pilatus 1M detector at a sample-detector distance of 2.85 m, a wavelength λ = 0.991 Å and an exposure time of 1 s/frame. A momentum transfer range of 0.036–0.50 Å^{-1} was covered ($q = 4\pi \sin\theta/\lambda$, θ being the scattering angle and λ the wavelength of the incident X-ray beam). Data collected during continuous sample flow through the capillary were subtracted from buffer scattering. The frames showing a negligible variation of the radius of gyration (R_g) were merged for further analysis.

R_g values were obtained from the Guinier approximation $sR_g < 1.3$ using Primus (29). Distance distribution functions $p(r)$ and the Porod volumes (V_ρ) were computed from the entire scattering curve using GNOM (30). Buffer subtraction and extrapolation to infinite dilution were performed by using the program package Primus (30) from the ATSAS 2.8.4 software suite. The forward scattering ($I(0)$) and the radius of gyration (R_g) were evaluated by using the Guinier approximation, and the maximum distance D_{max} of the particle was also computed from the entire scattering patterns with GNOM. The scattering from the crystallographic models was computed with CRYSOL (31). The volume fractions of the oligomers were determined with OLIGOMER (32), using as probe a set of two structural models corresponding to the monomer and the dimer, and a set of two PDBs corresponding to the dimer and the tetramer. The monomer, dimer and tetramer models were derived from structures presented herein.

Protein crystallization

Purified Rap_{pLS20} was concentrated to 10 mg/ml in 20 mM Tris–HCl pH 8, 250 mM NaCl, 10 mM MgCl$_2$, 1 mM EDTA, 1% (v/v) glycerol. Crystals of Rap_{pLS20} giving the highest resolution were obtained by the sitting-drop vapor-diffusion method at 18°C, by equilibration of drops of 1 μl protein + 1 μl crystallization buffer (10% (w/v) PEG6K, 0.1 M Hepes pH 7, benzamidine hydrochloride 0.1 M) against 100 μl of the crystallization buffer. Needle-shaped crystals were cryo-cooled in liquid nitrogen using a cryo-protecting solution containing reservoir solution supplemented with 20% (v/v) glycerol.

For crystallization experiments of the $Rap_{pLS20}/Phr^*_{pLS20}$ complex, the peptide was added to the diluted protein at a ratio of 1:5 ($Rap_{pLS20}/Phr^*_{pLS20}$) and the mixture was concentrated to 10 mg/ml in 20 mM Tris–HCl pH 8, 250 mM NaCl, 10 mM MgCl$_2$, 1 mM EDTA, 1% (v/v) glycerol. Crystals of Rap_{LS20}- Phr^*_{pLS20} were obtained by sitting-drop vapor-diffusion at 18°C, by equilibration of drops of 1 μl protein + 1 μl crystallization buffer (2.5% (w/v) PEG8K, 8% (v/v) ethylene glycol, 0.1 M MES pH 6.8) against 100 μl of the crystallization buffer.

Data collection was performed at ALBA synchrotron Light Source on the BL13-Xaloc beamline (33). The crystals of native Rap_{pLS20} belonged to space group $P2_12_12$ with two protein molecules in the asymmetric unit. The crystals of the $Rap_{pLS20}/Phr^*_{pLS20}$ complex belonged to space group C2, with four protein molecules in the asymmetric unit. Data were processed with AutoPROC (Global Phasing Ltd, (34)), using anisotropic resolution cutoffs (35). Data processing statistics are presented in Table 1.

Structure refinement

The TPR domain of the structure of the RapF protein with PDB code 4I9E (11) was used for molecular replacement by the program phaser (36). The native model of Rap_{pLS20} was then used for molecular replacement for the $Rap_{pLS20}/Phr^*_{pLS20}$ data. Crystallographic refinement of the models was done using phenix 1.12–2829 (37) and manual building in Coot (38), using the $2F_o - F_c$ and $F_o - F_c$ electron-density maps from refinement. Refinement statistics are presented in Table 1. Figures were prepared using PyMOL (The PyMOL Molecular Graphics System, Version 1.8 Schrödinger, LLC). Sequence and secondary structure were visualized using ESPript (39). The apo structure of Rap_{pLS20} was deposited as PDB code 6T3H and the peptide-bound structure was deposited as PDB code 6T46.

Superposition of Rap_{pLS20} monomers

To quantify changes in conformation between different, yet equivalent structures, the displacements of the equivalent atoms were expressed as a root-mean-square deviation (RMSD) of the atomic positions after superpositioning different parts of the structures. The main chain atoms of either the matching full length sequence (residues 9–361), or of residues 80-361 (CTD), or of residues 9–68 (NTD), respectively, of each of the crystallographically independent monomers of the Rap_{pLS20} apo and $Rap_{pLS20}/Phr^*_{pLS20}$ structures were superposed using the least squares algorithm implemented in Coot. The superposition of the main chain atoms of residues 268–361, corresponding to residues in H13-H17, was calculated using the *fit* command in Pymol. The *rms_cur* command in Pymol was used to calculate

Table 1. X-ray data processing and refinement statistics

Data processing statistics	Rap apo (6T3H)	Rap+Phr* (6T47)
Space group	$P\,2_1\,2_1\,2$	$C\,1\,2\,1$
Unit-cell parameters (Å)	$a = 111.790$, $b = 174.487$, $c = 49.879$	$a = 116.67$, $b = 93.28$, $c = 167.69$
Unit-cell angles (°)	$\alpha = \beta = \gamma = 90$	$\alpha = \gamma = 90$, $\beta = 94.97$
Resolution range (Å)[a]	87.2–3.04 (3.09–3.04)	45.4–2.450 (2.492–2.450)
No. of unique reflections	18645 (797)	63446 (3200)
Spherical completeness (%)	95.3 (82.5)	96.1 (96.8)
Ellipsoidal completeness (%)	95.3 (82.5)	95.9 (95.6)
Redundancy	4.6 (4.5)	2.2 (2.2)
Mean $I/\sigma(I)$	14.8 (1.4)	10 (0.3)
R_{meas} (%)[b]	7.5 (104.1)	4.4 (154.7)
Refinement statistics		
R_{work}[c] (%)	20.13	19.93
R_{free}[d] (%)	25.93	25.68
Ramachandran		
Favored (%)	92.95	96.4
Disallowed (%)	1.13	1.31
R.M.S.D.		
Bond lengths (Å)	0.004	0.01
Bond angles (°)	0.734	1.503
Chirality		
Mean B value (Å²)	95.4	73.3

[a]Numbers in parentheses represent values in the highest resolution shell.
[b]$R_{\mathrm{meas}} = \sum hkl\,[N/N-1]^{1/2}\sum_i |Ii(hkl) - <I(hkl)>|/\sum_{hkl}\sum_i Ii(hkl)$ where N is the multiplicity of a given reflection, $Ii(hkl)$ is the integrated intensity of a given reflection and $<I(hkl)>$ is the mean intensity of multiple corresponding symmetry-related reflections.
[c]$R_{\mathrm{work}} = \sum ||F_{\mathrm{obs}}| - |F_{\mathrm{calc}}||/\sum |F_{\mathrm{obs}}|$, where $|F_{\mathrm{obs}}|$ and $|F_{\mathrm{calc}}|$ are the observed and calculated structure factor amplitudes, respectively.
[d]R_{free} is the same as R_{work} but calculated with a 5% subset of all reflections that was never used in refinement.

the RMSD of the main chain atoms of residues 9–68 after superposition of residues 80–361.

RESULTS

This study shows that the oligomerization state of $\mathrm{Rap_{pLS20}}$ is concentration dependent. For the purpose of comparison, Supplementary Table S1 lists the concentrations used for the solution experiments.

Overall structure of $\mathrm{Rap_{pLS20}}$

The apo structure shows that $\mathrm{Rap_{pLS20}}$ is all α-helical, consisting of 17 antiparallel helices that are connected by short loops (Figure 1A and B). The C-terminal region consists of 14 helices forming 7 bi-helical TPR motifs, making up the typical solenoid structure associated with TPR folds (2). The solenoid covers more than a full turn, resulting in an interaction of the C-terminus with H5 and H6. The channel of the solenoid structure is open towards the N-terminus, but tightens towards the C-terminus, mainly due to the presence of the sidechains of residues R261 and W225.

The inner surface of the solenoid is lined by the even-numbered helices from H4 to H16 (Figure 1B), which form the pocket to which the peptide binds. The TPR topology is lost at the N-terminal end of helix H4, as helix H3 is located towards the inner lining and helix H2 towards the outer lining of the solenoid, an inversion with respect to helices H4 and H5. The loop between helices H3 and H4, indicated in red in Figure 1B, therefore marks the boundary between the NTD and the C-terminal TPR domain. This loop is the longest loop in the structure, consisting of 13 residues, and shows up poorly in the electron density maps, indicating a

high degree of flexibility. Helices 1–3 form an antiparallel three-helix bundle, where helices H1 and H3 interact with the N-terminal region of helix H4. Helix H2 packs with helix H1 and the opposing side of helix H3 is exposed to the exterior part of the protein.

The three helices of the NTD are approximately parallel and therefore do not form a HTH topology. Instead, their configuration resembles that of the TPR fold, but the domain is tilted with respect to the C-terminal TPR domain. The linker between helices 3 and 4 mentioned above provides the flexibility required for this change in orientation. This implies flexibility of the functionally important NTD domain, which relays peptide binding to a downstream response (6).

$\mathrm{Rap_{pLS20}}$ forms dimers in the packing of the crystal structure in a similar fashion to the *B. subtilis* phosphatase RapH (18). The interaction involves the protein surface of helices H5–H7 and H16–H17, including the C-terminal residues (Figure 1B and C). The N-terminal entrances of the channels of the solenoid structures face outwards with respect to the dimer interface. The buried solvent-accessible surface of the dimer interface in the apo structure is presented in Table 2. It is the largest buried surface area in the structure, and corresponds to the interface having the strongest interactions present in the structures according to strength indicators (see Table 2).

$\mathrm{Rap_{pLS20}}$ oligomerization state in solution

To determine whether the apo form of $\mathrm{Rap_{pLS20}}$ also forms dimers in solution as observed in the crystal structure, we carried out two complementary analytical ultracentrifugation (AU) approaches: sedimentation velocity (SV) and sedimentation equilibration (SE) experiments. In SV experi-
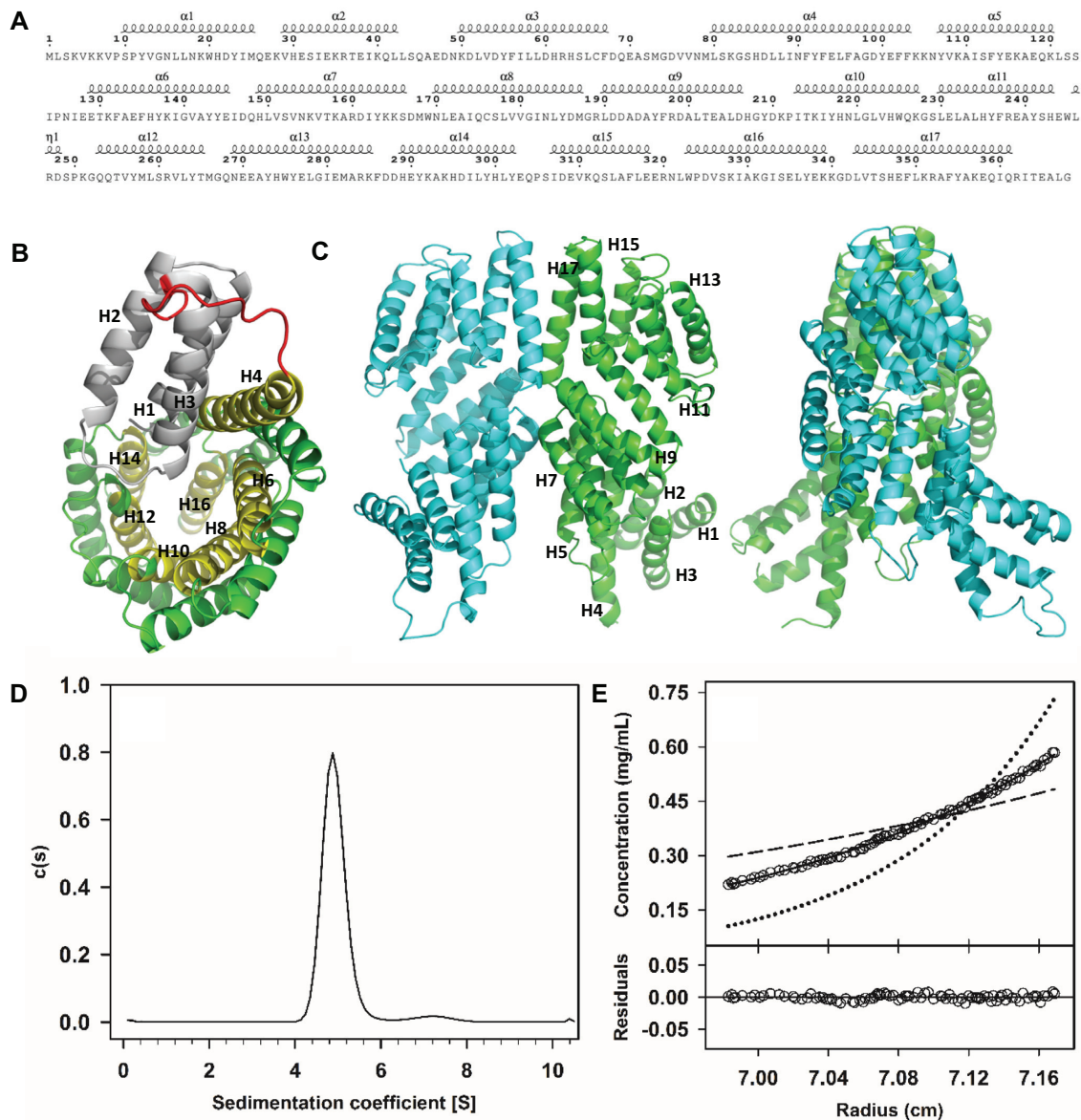
Figure 1. Overall crystallographic structure and ultracentrifuge results of apo Rap$_{pLS20}$. (**A**) Sequence and secondary structure of the apo structure. (**B**) N-terminal view of a cartoon representation of the apo Rap$_{pLS20}$ structure. Helices H1–H3 of the N-terminal domain are shown in gray, the H3–H4 loop in red and the even-numbered TPR helices lining the solenoid in yellow. Uneven-numbered helices are shown in green. (**C**) Cartoon representation of the side view of the dimeric structure of apo Rap$_{pLS20}$ in two orientations. (**D**) Sedimentation velocity assay showing the sedimentation coefficient distribution $c(s)$ corresponding to 4.5 μM (0.20 mg/ml) purified Rap$_{pLS20}$. (**E**) Sedimentation equilibrium assay. Upper part: concentration gradient of experimental data for Rap$_{pLS20}$ (empty circles) are presented together with best-fit analysis assuming protein monomer (dashed line), dimer (black line), or tetramer (dotted line) species. Lower part: Difference between experimental data and estimated values for a protein dimer model (residuals).

ments, more than 96% of Rap$_{pLS20}$ was observed as a single species with an experimental sedimentation coefficient of 4.9 S at 4.5 μM (0.20 mg/ml). This sedimentation coefficient, after correction to standard conditions (S20,w = 5.4S), was compatible with the theoretical mass of a slightly elongated Rap$_{pLS20}$ dimer ($f/f_0 = 1.3$) (Figure 1D). Since the apparent M_w obtained in SV analyses is influenced by the shape of the protein complex, we also performed SE experiments at concentrations ranging from 4.5 to 25 μM or 0.20 to 1.1 mg/ml (Figure 1E). The buoyant mass obtained was 22 930 ± 110 Da, corresponding to a molar mass of 89 970 ± 440 Da, using a partial specific volume of 0.7363, con-

firming that Rap$_{pLS20}$ (theoretical M_w of 44.4 kDa) behaves predominantly as a dimer in solution.

Structural comparison and evolutionary link

Given the low sequence homology among members of the RRNPP family (6), a comparison of the structure of Rap$_{pLS20}$ with other known structures in the PDB database could be very insightful (40). The full sequence of the apo structure was subjected to a PDB eFold search (41), summarized in Supplementary Table S2, in which the RRNPP proteins are grouped according to their function and source

Table 2. Relevant parameters indicating the strengths of the interface areas between the C-terminal TPR dimerization domains (CTD) and N-terminal tetramerization domains (NTD), respectively, for the different monomers in the asymmetric units in apo and peptide-bound Rap$_{pLS20}$ structures

Structure	Interactions	Area (Å^2)	ΔG	$\Delta G/P$	CSS
Rap Apo	CTD of Chain A with chain B	1432	−10.2	0.341	0.79
Rap Pep	CTD of Chain A with chain C	1606	−12.2	0.285	0.453
	CTD of Chain E with chain G	1440	−13.6	0.205	1.00
Rap Apo tetramer	NTDs of Chain A with chain B*	1347	−24.1	0.01	0.85
Rap Pep	NTDs of Chain G with chain E*	1207	−16.6	0.05	1.00
	NTDs of Chain C with chain A*	1306	−22.1	0.01	0.516

*The interaction is with the indicated chain of a symmetry-related molecule.

organism. The table is complemented with relevant RRNPP and non-RRNPP entries that were not identified by the eFold search. The search resulted in the retrieval of most but not all RRNPP proteins, indicating that there are significant structural differences between Rap$_{pLS20}$ and some RRNPP members, particularly in the NTD. Most interestingly, a number of non-related TPR proteins were found to have a greater structural similarity to Rap$_{pLS20}$ than some of the RRNPP proteins, suggesting that the RRNPP proteins and the non-RRNPP hits stem from a common ancestor. When investigating the structural similarities, it became clear that the evolutionary link between these proteins lies in the peptide binding function of the TPR domain. For example, human LGN is one of the proteins that were found to have a TPR domain that is structurally similar to RRNPP proteins. Human LGN is involved in mitotic spindle orientation of eukaryotic cell division, and in order to do so, it must be able to interact with different partner proteins (42,43) by binding to a polypeptide segment of each. However, the peptides to which LGN binds are generally much longer than the processed signaling molecules in bacterial quorum sensing, and RRNPP proteins are unable to bind long peptides because the peptide binding site at the C-terminus forms a cul-de-sac in which only short peptides are able to fit. A second functionally and structurally important adaptation between RRNPP and LGN is related to the NTD, which is absent in LGN.

Fluorescence polarization binding assay

We have determined by fluorescence anisotropy the affinity of a synthetic Phr*$_{pLS20}$ peptide to Rap$_{pLS20}$ using a competition assay between a chromophore-labelled (6-FAM-Phr*$_{pLS20}$) and an unlabeled Phr*$_{pLS20}$ peptide following a previously described protocol (44). Briefly, fluorescence anisotropy was measured for samples containing fixed concentrations of Rap$_{pLS20}$ and 6-FAM-Phr*$_{pLS20}$ and increasing concentrations of native Phr*$_{pLS20}$. The binding data obtained in these fluorescence polarization assays were fitted (Figure 2A) to the Hill-Langmuir equation (45), resulting in a Hill coefficient of 1 (no cooperativity in the interaction). The determined IC$_{50}$ was 26.73 ± 0.27 μM, which corresponds to a K_D value of 7.42 μM, which is in the same range as the 3.1 μM K_D value calculated for the RapF-PhrF* pair (11), but significantly less than the 0.03 μM calculated for NprR and its cognate peptide NprX (46). The difference in peptide affinity between Rap proteins and NprR may be explained by the difference in length of the peptide (five amino acids for the Phr peptides and eight for

NprX). The K_D value allowed us to estimate the proper ratio of Rap$_{pLS20}$/Phr*$_{pLS20}$ required to obtain high percentage of protein bound to the peptide. Unless stated otherwise, a ratio of 1:5 (Rap$_{pLS20}$:Phr*$_{pLS20}$) was chosen for the experiments described herein, as under these conditions a 98.8% Phr*$_{pLS20}$ was calculated to be bound to the protein.

Structures of peptide-bound Rap$_{pLS20}$

Having resolved the structure of the apo form, we were interested in revealing the structural effects of Phr*$_{pLS20}$ binding on Rap$_{pLS20}$. Crystals diffracting at 2.45 Å were obtained, and X-ray analyses revealed that the peptide-bound Rap$_{pLS20}$ crystallized in a different space group with distinct cell parameters (see Table 1), consisting of four independent chains in the asymmetric unit. The electron density of the peptide was clearly observed in all chains (Supplementary Figure S1). The approximate location and orientation of the peptide in the TPR domain of Rap$_{pLS20}$ is preserved compared with other members of the RRNPP family (not shown). The peptide is oriented along the solenoid axis of the TPR domain, with its N-terminus bound in a closed pocket pointing towards the C-terminus of Rap$_{pLS20}$. The C-terminus of the peptide, however, points towards an open channel, which provides clues about how the peptide enters the active site. Interestingly, superpositions with other RRNPP-peptide structures show that small relative displacements of the peptide occur along the solenoid direction (not shown). Recognition of the peptide by Rap$_{pLS20}$ involves residues from helices H6, H8, H10, H12, H14 and H16 (Figure 2B).

The sequence of the mature Phr*$_{pLS20}$ peptide corresponds to the last five amino acids of the pre-proprotein, residues forty to forty-four, with the sequence QKGMY. Phr*$_{pLS20}$ adopts an extended conformation, with residues Q40 and K41 pointing in opposite directions with respect to the main chain, as do residues M43 and Y44 (Figure 2B). Thus, residues K41 and Y44 point towards helix H6, whereas Q40 and M43 point towards the interface between helices H10 and H12. K41 interacts with residues at the top of helix H6. This part of H6 interacts in turn with helices H16 and H17, which are involved in the dimer interface. The peptides of the four monomers of the peptide-bound Rap$_{pLS20}$ structure were superposed to visualize the movement of Rap$_{pLS20}$ structural elements with respect to the peptide. This analysis shows that in one of the Phr*$_{pLS20}$-bound chains, the C-terminal helices H13-H17 of the TPR moves downwards by 2.6 Å, bringing these helices close to the helices H5–H7.
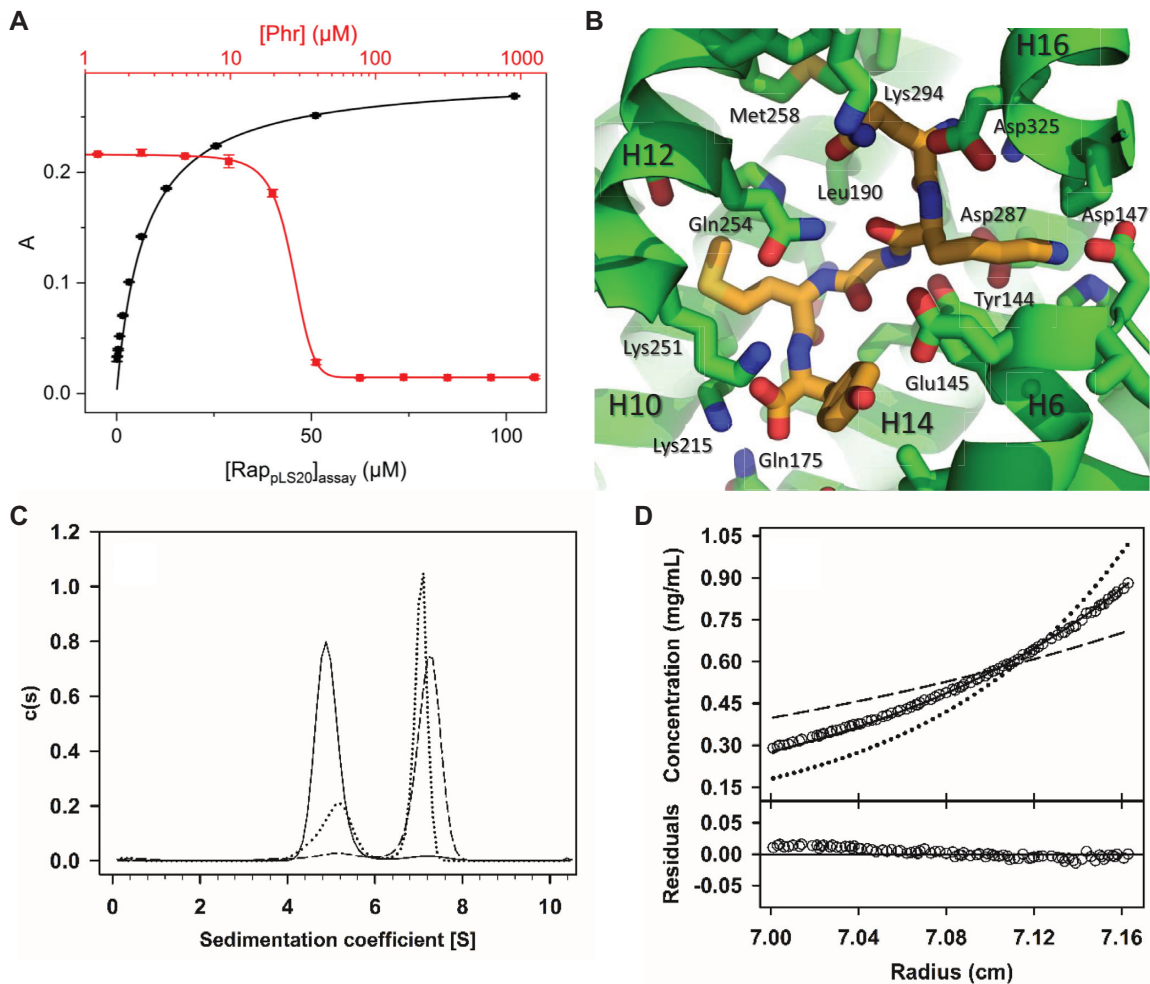
Figure 2. Interaction of the Phr*$_{pLS20}$ peptide with Rap$_{pLS20}$. (**A**) Rap$_{pLS20}$/Phr*$_{pLS20}$ binding affinity as determined by fluorescence polarization. The black-colored data points resresent the fluorescence polarization of the 6-FAM-labeled Phr*$_{pLS20}$ peptide as a function of Rap$_{pLS20}$ concentration. The red-colored data points shows the results of a fluorescence anisotropy competition assay with unlabeled Phr*$_{pLS20}$. The black and red lines represent the fit of the experimental data to the Hill equation for a single binding site. Error bars represent standard deviations from four samples. (**B**) Stick representation of the crystal structure of the peptide-bound crystallographic structure, showing the carbon atoms of the peptide in orange and those of Rap$_{pLS20}$ in green. Interacting residues of Rap$_{pLS20}$ are indicated. (**C**) Sedimentation coefficient distributions, $c(s)$, obtained from SV assays at 280 nm with 4.5 μM of apo Rap$_{pLS20}$, showing the shift in the *s*-value of this protein after addition of Phr* at 4.5 μM (dotted line) or 15 μM (dashed trace) relative to Rap$_{pLS20}$ alone (solid trace). (**D**) Sedimentation equilibrium assay. Upper part: concentration gradient of experimental data for Rap$_{pLS20}$ with Phr*$_{pLS20}$ at 15 μM (empty circles) are presented together with best-fit analysis assuming protein dimer (dashed line), tetramer (black line) or hexamer (dotted line) species. Lower part: Difference between experimental data and estimated values for the protein tetramer model (residuals).

The superpositions of the peptides revealed a significant degree of freedom of movement, which was further analyzed by superposing the structural elements of the protein. For this, the different chains of both the apo Rap$_{pLS20}$ and Rap$_{pLS20}$ peptide-bound structures were superposed (Supplementary Tables S3 and S4). To get insight into the structural changes induced in Rap$_{pLS20}$ due to peptide binding, we calculated the average distance existing between the main chain atoms of the apo- Rap$_{pLS20}$ structure to the equivalent main chain atoms of the superposed Phr*$_{pLS20}$– Rap$_{pLS20}$ structure, and expressed these as RMSDs. The superposition of all possible residues showed that the overall structure did not change much, evidenced by the fact that the RMSDs ranged from 1.33 to 3.54 Å (Supplementary Table S3). However, visual inspection of these superpositions

suggested that the orientation of the NTDs changed relative to the CTDs. We therefore superposed only the CTDs of the apo and peptide-bound monomers (RMSDs of 0.58–2.86 Å) and the NTDs of all monomers (RMSDs of 0.64–1.50 Å) (see Supplementary Table S3). In addition, we calculated the RMSDs of the NTDs after superposition of the CTDs, which were in the range of 1.30 to 7.0 Å (Supplementary Table S4). The significant increase in the RMSDs of the NTDs after superposition of the CTDs compared to those of the superposition of the NTDs confirmed the change in relative orientation of the domains. We found that in the presence of the peptide, the NTDs move in a single direction and have a tendency to swing outward, away from the solenoid axis of the TPR. This movement can be observed to various degrees and was most pronounced for two of the

four monomers (chains C and G) in the Phr*$_{pLS20}$–Rap$_{pLS20}$ structure, which each belong to the two different respective dimers.

To delineate further which regions were relatively rigid or flexible, superpositions of subsets of the helices of the CTDs were performed and inspected visually. These analyses showed that the C-terminal helices H13–H17 were invariant when compared to the preceding structural elements, as evidenced by RMSDs of 0.380–0.740 Å after the superposition of helices H13-H17 (residues 268–361) of all monomers of the apo and peptide-bound structures (Supplementary Table S3). The superposition revealed that helices H6 and H7 (residues 129–166) of the TPR domain move inwards towards the center of the solenoid where the peptide binds, and upwards towards the C-terminus. The extent of this movement is distinct for the four chains of the Phr*$_{pLS20}$-bound Rap$_{pLS20}$ and ranges from 2.1 to 3.5 Å. This ample range of movement confirms that the TPR domain retains a high level of flexibility in the presence of the bound peptide. The movements in helices H6 and H7 are related to an outward movement of the N-terminal 3-helix bundle. In fact, the extent of both movements is correlated: the N-terminal bundles swing out over a larger distance when the TPR rearrangement is more pronounced. The correlation between the displacement of helices H6 and H7 and the tendency of the NTDs to move outward is likely functionally important for the response of Rap to the peptide. Figure 3A shows the positions of the effector domain with respect to the TPR domain for one monomer of the apo structure (chain B) and one monomer of the peptide-bound structure (chain G).

Effect of Phr*$_{pLS20}$ on Rap$_{pLS20}$ oligomerization in solution

To investigate possible effects of peptide binding on the oligomerization state of Rap$_{pLS20}$ in solution, we performed SV and SE ultracentrifugation experiments of Rap$_{pLS20}$ in the presence of synthetic Phr*$_{pLS20}$. Interestingly, the presence of Phr*$_{pLS20}$ induced a change in oligomerization state of Rap$_{pLS20}$ in a dose-dependent manner, resulting in the formation of Rap$_{pLS20}$ tetramers. At a 1:1 stoichiometry, there was still a small trace of Rap$_{pLS20}$ dimers, which was no longer observed when the peptide was present in excess with a 3:1 stoichiometry. Thus, an equilibrium between the dimer and tetramer was observed, as was the case for apo Rap$_{pLS20}$. In fact, in the absence of the peptide, a small but measurable concentration-dependent presence of tetramers was observed in SV experiments of apo Rap$_{pLS20}$, which increased from 1.1% at 4.5 μM (0.20 mg/ml) to 3.6% at 25 μM (1.1 mg/ml).

SV assays showed a shift of the sedimentation coefficient of Rap$_{pLS20}$ from 4.9 S, corresponding to the protein dimer, to an s-value of 7.1 S, compatible with a slightly elongated shape of the Rap$_{pLS20}$ tetramer ($f/f_0 = 1.44$) (Figure 2C). To confirm the oligomerization state of Rap$_{pLS20}$ in the presence of the peptide, regardless of the hydrodynamic shape, we carried out a SE experiment of Rap$_{pLS20}$ at different concentrations (0–15 μM or 0–0.67 mg/ml) in the presence of a 1:3 stoichiometry (Rap$_{pLS20}$:Phr*$_{pLS20}$). SE showed a buoyant mass of 44 300 Da, corresponding to a molar mass of 174 000 ± 740 Da, in good agreement with the expected

M_w for the protein tetramer (Figure 2D). Together, these data show that Rap$_{pLS20}$ forms tetramers in solution in the presence of Phr*$_{pLS20}$.

The tetramerization interface of Rap$_{pLS20}$

We next checked if tetramerization of Rap$_{pLS20}$ observed by AUC is also reflected in the crystal structures. When analyzing the intermolecular contacts in the peptide-bound crystal structure, we found an additional interface that explains the tetrameric configuration of Rap$_{pLS20}$, which surprisingly was also found in the structure of the apo form. This second interface formed through interactions between the helices 3 of the NTDs of the interacting molecules, and by insertion of the N-terminus of helix H4 between helices H4-6 and the N-terminus of helix H3 of the opposite molecule. We will refer to this interaction as the **foot-2-foot interaction** (Figure 3B and C). Of the many interactions found in the interface, we highlight here M79 and L80 located in H4 (Figure 3D), which forms part of the CTD and interact substantially with residues in the H4–H5 loop of the opposing monomer. Within the PSI-BLAST (47) set of proteins, which includes Rap$_{pLS20}$-like proteins, we found that L80 is highly conserved (I, L or V in homologous proteins) and sits in a hydrophobic pocket lined with residues F91, Y92, L121, P125, I127, K131 of a chain from the opposite dimer. Of these interacting residues, F91-Y92 are 100% identical among the BLAST sequences, and 121 is mainly L with a smaller percentage of I. In addition, P125 and I127 are very well conserved (mainly P, then A/E/D/T for P125 and 100% for I127). K131 is Q in most sequences, followed by K, then smaller populations of Y, H, R. Interestingly, within the 11 Rap proteins of *B. subtilis*, the conservation of the residues forming this pocket is much smaller. Except for F91-Y92 and L121, the remaining pocket residues and L80 and the preceding loop, containing M79, are poorly conserved. This may indicate that peptide-induced tetramerization is common among Rap$_{pLS20}$-like proteins, but does not occur among the genomic *B. subtilis* Rap proteins characterized so far.

Table 2 gives the interface strengths for the tetramer interfaces in the apo structure (one crystallographically independent interface) and the peptide-bound structure (two crystallographically independent interfaces). The strength of the interface area of the foot-2-foot interactions shows that the N-terminal interactions are viable interactions that are stronger than other contacts in the crystal lattice.

SAXS analysis of the particle size of Rap$_{pLS20}$ and Rco$_{pLS20}$, with and without Phr*$_{pLS20}$

We have established the formation of Rap$_{pLS20}$ tetramers using AUC and we have derived a possible interface of this interaction from the crystal structures. The contacts observed in the crystal surface could be crystallographic artefacts, though, that may not occur in solution. Therefore, this interface required confirmation, using different techniques to provide additional insights into the oligomerization behavior and shape of Rap$_{pLS20}$ in solution in the presence and absence of the Phr*$_{pLS20}$ peptide. Multiple size exclusion chromatography (SEC) and SAXS analyses were performed on (combinations of) Rap$_{pLS20}$, Rco$_{pLS20}$ and Phr*$_{pLS20}$.
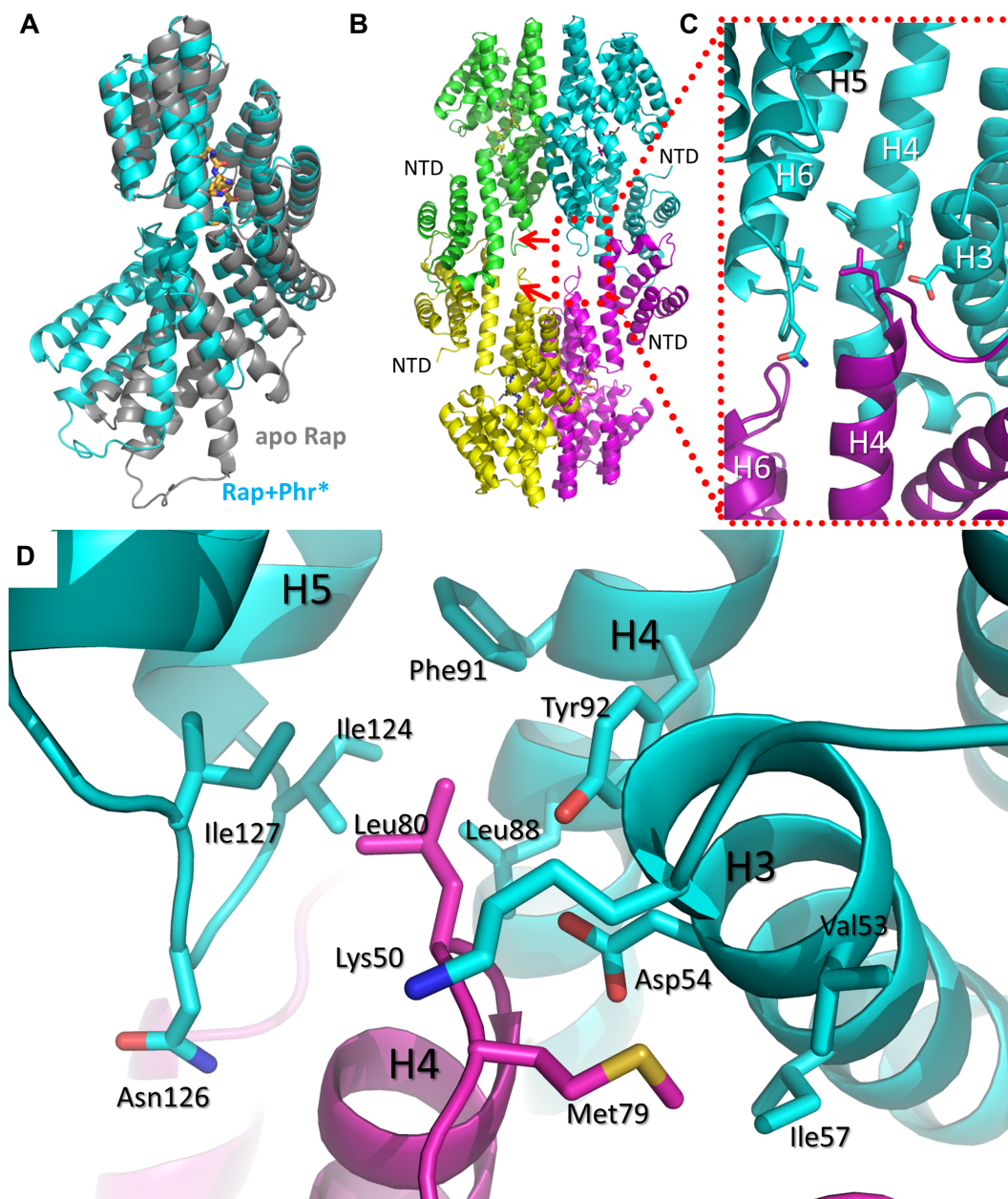
Figure 3. Rap$_{pLS20}$ tetramerization. (**A**) Cartoon representation of the superposition of the C-terminal domains of one of the peptide-bound chains (cyan) on one of the apo chains (gray), highlighting The shift in the N-terminal domain (NTD). The peptide carbon atoms are shown in orange. (**B**) Side view of the peptide-bound tetramer. The red arrows indicate the loops connecting helices H4 and H5. (**C**) Zoom of the area around the N-terminus of helix H4, showing the insertion of this helix into the opposite monomer. (**D**) Close up view of the hydrophobic pocket of M79 and L80 in the formation of the tetramer.

We analyzed apo Rap$_{pLS20}$ at concentrations of 11 μM to 0.11 mM (0.5–5 mg/ml) and Rco$_{pLS20}$ at concentrations of 70.9–709 μM (1.44–14.4 mg/ml), both in the absence and presence of Phr*$_{pLS20}$ at a 5× molar excess. A summary of the most important global SAXS parameters is given in Table 3.

Comparison of SAXS data obtained for Rap$_{pLS20}$ showed that the presence of Phr*$_{pLS20}$ provoked an increase in the volume and weight of Rap$_{pLS20}$ particles (Table 3). The presence of the peptide resulted in the following specific increases: the radius of gyration increased from 3.8 to 4.5

nm; the Porod volume increased from 195 to 231 nm^3; and the maximum distance derived from the $P(r)$ changed from 14.6 to 14.8 nm. These data are consistent with a tetrameric Rap$_{pLS20}$/Phr*$_{pLS20}$ oligomerization as observed by AUC data and the X-ray structures.

The size indicators obtained for Rco$_{pLS20}$ at a concentration of approximately 1.44 mg/ml (70.9 μM), were similar to those obtained for Rap$_{pLS20}$ (Table 3). This indicates that Rco$_{pLS20}$ (theoretical M_w of 20.3 kDa) has a similar effective size as Rap$_{pLS20}$ (theoretical M_w = 44.4 kDa) in solution, consistent with AUC data published previously show-

Table 3. SAXS data obtained for samples of Rap_{pLS20}, Rco_{pLS20}, or mixed samples in the absence and presence of $Phr*_{pLS20}$. The average value obtained from curves at different concentrations are given, the values in brackets correspond to the highest and lowest values determined for the different concentrations

Sample	$Phr*_{LS20}$	R_g (nm)	V_{porod} (nm^3)	R_{max} (nm)
Rap_{pLS20}	−	3.8 (3.44–4.03)	195 (162–217.5)	14.6 (14.3–14.9)
	+	4.5 (4.21–4.52)	231 (174.1–263.5)	14.8 (14.0–16.0)
Rco_{pLS20}	−	(4.52–6.19)	(206–443)	(15.8–21.7)
Rap_{pLS20}/Rco_{pLS20}	−	(5.3–11.9)	(294–1281)	(18.5–60.4)
	+	(4.35–4.86)	(255–286)	(15.0–17.0)

ing that Rco_{pLS20} is a tetramer in solution (23), and the AUC presented herein showing that Rap_{pLS20} behaves as a dimer. At higher concentrations, however, the parameters indicate that the effective size of the particles increase, suggesting that Rco_{pLS20} forms complexes of higher M_w at increasing concentrations.

SEC and SAXS analysis show that the Rap_{pLS20}-Rco_{pLS20} complex is disrupted by $Phr*_{pLS20}$

Since we were also interested in studying the interaction between Rap_{pLS20} and Rco_{pLS20} and the effect of the signaling peptide on this possible interaction, we measured scattering curves of mixtures of Rap_{pLS20} and Rco_{pLS20} at different stoichiometries and concentrations, in the absence and presence of $Phr*_{pLS20}$ (Table 3). In the absence of signaling peptide, mixtures of Rap_{pLS20} and Rco_{pLS20} exhibited a several-fold increase in all particle size indicators, independent of their relative stoichiometries. This shows that a complex between Rap_{pLS20} and Rco_{pLS20} is indeed formed, confirming direct interaction between these proteins. When mixtures of Rap_{pLS20}, Rco_{pLS20} and $Phr*_{pLS20}$ were analyzed by SAXS, the overall indicators of particles size and shape (Table 3) were similar to those of the Rco_{pLS20} protein alone and the Rap_{pLS20}/$Phr*_{pLS20}$ complex, regardless of the relative concentrations of the components.

Next, we analyzed the oligomerization behavior of Rap_{pLS20} and Rco_{pLS20} using analytical size exclusion chromatography (SEC) at a total protein concentration ranging between 0.75 and 1.25 mg/ml and estimated the M_w of the different complexes based on a calibration using proteins of known M_w (Supplementary Table S5). The results show that Rap_{pLS20} and Rco_{pLS20} alone eluted at similar volumes, with estimated weights of 101 and 94.4 kDa, respectively, corresponding to Rap_{pLS20} dimers and Rco_{pLS20} tetramers. The formation of apo Rap_{pLS20} dimers in solution is in agreement with AUC data reported above and with previously reported SEC results (48). The tetrameric form of Rco_{pLS20} is in agreement with AUC results reported before (23), but does not agree with previously published SEC and sucrose gradient results (48).

As mentioned above, higher order complexes were observed by SAXS for mixtures of Rap_{pLS20} and Rco_{pLS20} in absence of the signaling peptide. SEC experiments of mixtures of Rap_{pLS20} and Rco_{pLS20} showed similar results (Supplementary Figure S2C–F). Addition of $Phr*_{pLS20}$ to the Rap_{pLS20} and Rco_{pLS20} mixtures disrupted these higher order complexes in SEC (Supplementary Figure S2H), in agreement with SAXS results. Together, the SAXS and SEC

data are consistent with $Phr*_{pLS20}$-dependent disruption of Rco_{pLS20}–Rap_{pLS20} complexes and concomitant formation of a Rap_{pLS20} tetramer.

SAXS confirms the formation of apo Rap_{pLS20} dimers and Rap_{pLS20}/$Phr*_{pLS20}$ foot-2-foot tetramers in solution

In order to assess the agreement between X-ray structure and SAXS data, models of the monomer, dimer and tetramer from the crystal structures were used to calculate a fit with the SAXS scattering curves (Supplementary Table S6). Based on the crystal lattices, two different tetramer models were generated: one representing a foot-to-foot induced tetramer, and the second generated using (weaker) side-to-side CTD interactions found in the crystal structures. SAXS data of Rap_{pLS20} showed that at all tested concentrations, the best model to explain the curves was always a combination of dimer (Figure 1C) and foot-2-foot tetramer (Figure 3B). Unacceptable fits were invariably obtained for combinations of the Rap_{pLS20} monomer, the dimer and for the CTD-based, side-to-side tetramer (Supplementary Figure S3 and Supplementary Table S4). The best fit for the apo Rap_{pLS20} SAXS curve at 0.5 mg/ml (11.3 μM) was obtained with a dimer:tetramer ratio of 0.78:0.22. The percentage of foot-2-foot tetramers increased at higher Rap_{pLS20} concentrations; e.g. at 5 mg/ml (0.11 mM) the Rap_{pLS20} dimer:tetramer ratio was 0.48:0.52 (Figure 4 and Supplementary Table S6). Thus foot-2-foot tetramers are found to coexist with dimers in solutions of apo Rap_{pLS20}, and their proportion depended on the Rap_{pLS20} concentration.

Importantly, the presence of $Phr*_{pLS20}$ caused a considerable increase in the percentage of Rap_{pLS20} tetramers, which was particularly noticeable at low concentrations of Rap_{pLS20} (Figure 4). For example, at 0.5 mg/ml (11.3 μM) the presence of the signaling peptide caused the percentage of tetramers to increase from 22 to 75%. It is also worth noting that, as was the case for apo Rap_{pLS20}, the proportion of tetramers was augmented at increasing peptide-bound Rap_{pLS20} concentrations (maintaining the stoichiometries between Rap_{pLS20} and $Phr*_{pLS20}$ constant). In fact, 100% of Rap_{pLS20} was in tetramer form at Rap_{pLS20} concentrations above 2.5 mg/ml (57.7 μM). In summary, the SAXS data and the results of the ultracentrifugation experiments described above show that, in the absence of the peptide, Rap_{pLS20} has a tendency to form foot-2-foot tetramers at high concentrations. However, formation of these tetramers is strongly enhanced by the presence of the signaling peptide (Figure 4).
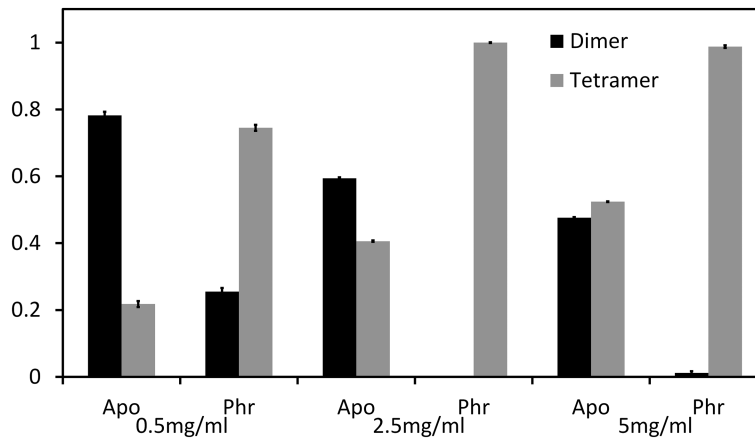
Figure 4. SAXS determined concentration-dependent dimer:tetramer stoichiometry of the apo and peptide-bound form of Rap$_{pLS20}$. The vertical bars represent the proportion of dimers and foot-2-foot tetramers of Rap$_{pLS20}$ and Rap$_{pLS20}$/Phr*$_{pLS20}$ samples at three different concentrations, as calculated with OLIGOMER ([32]).

DISCUSSION

Oligomerization state of Rap$_{pLS20}$

In a previous study, we demonstrated that Rap$_{pLS20}$ activates expression of conjugation genes by relieving Rco$_{pLS20}$-mediated repression of the main conjugation promoter P$_c$, and that this anti-repression activity of Rap$_{pLS20}$ is inhibited by Phr*$_{pLS20}$ ([22]). The results of the different experimental approaches applied in these studies show that Rap$_{pLS20}$ forms dimers which have an intrinsic ability to produce tetramers, but that tetramer formation is particularly stimulated by the cognate mature signaling peptide Phr*$_{pLS20}$. These results strongly suggest that tetramerization is a crucial feature for inactivation of Rap$_{pLS20}$. In the crystal structure, we observed two possible modes by which Rap$_{pLS20}$ may tetramerize. The solution experiments allowed the identification of the functional configuration of the Rap$_{pLS20}$ tetramerization, which we named the foot-2-foot interaction. Interestingly, in this complex, the dimer-dimer interface involves mainly interactions between the NTDs. This proposed model of the tetramer is also compatible with AUC data, since the frictional ratio indicates a slightly elongated model for the dimer and an even more elongated model for the tetramer. The deviations in the M_w estimations from SEC data may indicate non-globular molecular shapes and therefore also agree with the dimer and foot-2-foot models proposed by us.

The foot-2-foot interfaces seem to be stronger in the apo crystal structure compared to the peptide-bound structure (see Table [2]). There are several possible explanations for this observation. First, the resolution of the apo structure is higher and the electron density of the loop region is clearer, allowing a better positioning of the interacting residues. Second, the lower resolution of the peptide-bound structure may obscure bridging water molecules and ions, which would increase the strength of the interaction surface. And third, crystal contacts may push the NTDs to a non-preferred orientation in the apo structure that favors tetramer formation. However, our combined data based on results from different techniques provide compelling evidence that Phr*$_{pLS20}$ binding enhances Rap$_{pLS20}$ homotetramerization via a foot-2-foot interaction. Notably, AUC and SAXS experiments showed that Rap$_{pLS20}$ foot-2-foot tetramers can also form in solution in the absence of the signaling peptide, and that the proportion of the tetramers is concentration dependent. Our data therefore suggest that Rap$_{pLS20}$ dimers and tetramers are in a concentration-dependent equilibrium that is shifted in favor of the tetramer upon peptide binding.

Interaction between Rap$_{pLS20}$ and Rco$_{pLS20}$ in presence and absence of Phr*$_{pLS20}$

Our SAXS results firmly establish that Rap$_{pLS20}$ and Rco$_{pLS20}$ interact to form larger complexes, as indicated by the increase in particle size in solution. Interestingly, Rap$_{pLS20}$/Rco$_{pLS20}$ mixtures additionally containing Phr*$_{pLS20}$ yielded particle size parameters in the same range as those obtained for the Rap$_{pLS20}$/Phr*$_{pLS20}$ complex and Rco$_{pLS20}$ alone, indicating that Phr*$_{pLS20}$ interferes with interactions between Rap$_{pLS20}$ and Rco$_{pLS20}$. These data were corroborated by SEC, and overall show that Phr*$_{pLS20}$ restores the repressive action of Rco$_{pLS20}$ ([22,23]) by modulating the direct interaction between Rap$_{pLS20}$ and Rco$_{pLS20}$.

By extrapolating the fact that the NTD of RRNPP proteins determines their functionality, Rap$_{pLS20}$ and Rco$_{pLS20}$ interact most likely through the NTD of Rap$_{pLS20}$. There is a similarity to the RapF/ComA system, in that ComA and Rco$_{pLS20}$ are both DNA binding proteins that harbor an HTH domain. RapF binds ComA through a surface that mimics the surface of DNA ([16]). This interaction is mediated partly through a 27-residue linker that connects the NTD to the CTD ([16]). However, the corresponding linker in Rap$_{pLS20}$ is 14 residues shorter, and the electrostatic surface of Rap$_{pLS20}$ does not show pronounced negative charges. These observations indicate that the NTD of Rap$_{pLS20}$ does not likely mimic DNA, suggesting that Rap$_{pLS20}$ binds to its modulator protein Rco$_{pLS20}$ in a very different way. A possible implication of this is that Rap$_{pLS20}$ may not interact with the Rco$_{pLS20}$ N-terminal DNA-binding domain, but rather with its CTD, which resembles the lambda-phage C1 repressor (Interpro IPR010982 fam-

ily). Future structural studies will be performed to determine how Rco_{pLS20} interacts with Rap_{pLS20}.

Complex formation of RRNPP proteins compared with Rap_{pLS20}

Dimerization like that observed here in Rap_{pLS20} has been observed in the apo form of RRNPP proteins that bind DNA such as PlcR and PrgX, but is uncommon for other Rap proteins. Most Rap proteins have been reported to be monomers in solution, including RapF, RapH and RapK (16), and RapJ (17). RapH, however, does form dimers (18). For RapF (16) and RapJ (17), large conformational changes in the N-terminus have been observed in peptide binding, but no related changes in oligomerization state have been reported. In these Rap proteins, a large internal conformational change was proposed to account for the functional effects of peptide binding. In contrast, a change in oligomerization state was found for PlcR (4) and PrgX (49,50) upon peptide binding. The effect of peptide binding was, however, distinct for the two proteins: PlcR tetramerized upon peptide binding, whereas the two different peptides that compete for PrgX binding have stabilizing and destabilizing effects on tetramerization, respectively. Interestingly, the SAXS results of PlcR showed an extended volume, indicating formation of higher order oligomerization. At low protein concentrations, these volumes resemble to a great extent the foot-2-foot tetramers presented herein and were interpreted as tetramers, albeit through interactions in the N-terminal part of the TPR domain (4).

In Rap_{pLS20}, binding of the peptide results in changes of several alpha helices of the TPR domain, which in turn translates into changes in orientation of the NTDs such that they allow foot-2-foot interactions between opposing NTDs. In the peptide-bound structure, two crystallographically independent tetramer configurations were found, which are formed through foot-2-foot interactions between two symmetry-related dimers. In each of the tetramers, one of the NTDs moves outwards, thereby modifying the interaction interface. In the tetramer formed by chains G and E and their symmetry-related counterparts, the displacement of the NTD of chain G is most pronounced. In the tetramer formed by chains A and C and their symmetry-related counterparts, displacement of the NTD of chain C is most pronounced, but this displacement is smaller than that of chain G. The combined effect in the G/E tetramer is a stronger interaction than that observed for the A/C tetramer, judged by the strength of the buried surface area (Table 2). Curiously, the strength of the dimer interface in both peptide-bound tetramers is slightly decreased, suggesting that peptide weakens the dimer interface (Table 2).

The movement of the NTD with respect to its CTD observed here for Rap_{pLS20} upon $Phr*_{pLS20}$ peptide binding has also been observed for other members of the Rap family, such as RapF (PDB code 4i9c), RapJ (4gyo) and NprR (5dbk). Intriguingly, the movement of the NTD of Rap_{LS20} is opposite to that observed in these other structures. In fact, RapJ (17) and RapF (11) contract upon peptide binding, causing the N-terminal bundle to merge with the TPR domain. The position of the NTDs in these structures is not compatible with the tetrameric structures observed for

Rap_{pLS20}. The fact that a tetrameric oligomerization state is not observed for RapJ and RapF is consistent with this observation.

Tetramers of RRNPP proteins have been observed using a range of techniques, but atomic models of tetramers have been proposed only for NprR and PrgX. In PrgX, tetramerization has been proposed to occur through the CTDs of the apo protein (51). PrgX tetramers are destabilized upon binding of the cognate cCF10 peptide, so this mechanism is very distinct from the mechanism proposed here for Rap_{pLS20}. For NprR, however, the NTDs are important for the formation of tetramers, and the dimer-to-tetramer transition is induced by the peptide (46). The peptide-dependent transformation from dimer to tetramer of NprR is reminiscent of the behavior of Rap_{pLS20}. The interactions in the NprR tetramer occur between the TPR and NTD domains, though foot-2-foot interactions like those observed for Rap_{pLS20} were not found for the peptide-bound structure of NprR. Instead, the dimers are rotated 90° with respect to each other, and the NTDs bind on the sides of the TPR domains. Interestingly, the NTDs in the peptide-bound NprR structure move inward as is the case for the monomeric RapF and RapJ; however, this does not lead to tetramers for these Rap proteins.

The foot-2-foot tetramerization observed exclusively for Rap_{pLS20} may be the consequence of the very different NTD of this protein. Interestingly, interactions between the helices immediately following the NTDs are a common theme between the tetramerization interactions of Rap_{pLS20} and of the other types of interactions described above for other members of the RRNPP family, suggesting that this part of the TPR domain is of direct importance in translating peptide binding into a functional effect.

Implications of the mechanism of Rap_{pLS20}

The homotetramerization caused by the foot-2-foot interactions of the NTDs of Rap_{pLS20} provides an explanation for the activation of the Rco_{pLS20} partner (Figure 3). In the absence of $Phr*_{pLS20}$, the NTDs are positioned such that they allow the interaction with Rco_{pLS20}. However, upon binding the signaling peptide, the NTDs shift outwards, facilitating the formation of the homotetramer, leading to a change of the interaction surface of the NTDs that is no longer available for interactions with Rco_{pLS20}. This change leads to a release and subsequent reactivation of Rco_{pLS20}, which is again able to bind to the P_c (22). Thus, the structural changes introduced in the Rap_{pLS20} structure determine whether the conjugation process will be activated or not.

In summary, our approach combining four different techniques has been crucial in the elucidation of the oligomerization behavior of Rap_{pLS20} and its interaction partners. We have determined the X-ray structures of apo Rap_{pLS20} and the $Phr*_{pLS20}$-bound structure. These structures demonstrated that binding of the peptide changes the position of the NTDs with respect to the CTDs and result in a transition of homodimers to homotetramers of Rap_{pLS20}, through a foot-2-foot interaction between the repositioned NTDs. SAXS, SEC and AUC experiments confirm this model, which differs substantially from the

model proposed for other RRNPP family members. The differences in peptide-dependent oligomerization behavior seem to be closely related to the function of the NTDs of Rap proteins. Thus, the main (and possibly only) function of the C-terminal TPR domain seems to be in binding the peptide, whereas the NTD is responsible for exerting the biological function of the protein in response to binding of the cognate peptide.

DATA AVAILABILITY

Atomic coordinates and structure factors for the Rap$_{pLS20}$ and the Rap$_{pLS20}$ peptide-bound crystal structures have been deposited in the Protein Data bank under accession numbers 6T3H and 6T46, respectively.

SUPPLEMENTARY DATA

Supplementary Data are available at NAR Online.

REFERENCES

1. Rutherford,S.T. and Bassler,B.L. (2012) Bacterial quorum sensing: its role in virulence and possibilities for its control. *Cold Spring Harb. Perspect. Med.*, **2**, a012427.
2. D'Andrea,L.D. and Regan,L. (2003) TPR proteins: the versatile helix. *Trends Biochem. Sci.*, **28**, 655–662.
3. Lamb,J.R., Tugendreich,S. and Hieter,P. (1995) Tetratrico peptide repeat interactions: to TPR or not to TPR? *Trends Biochem. Sci.*, **20**, 257–259.
4. Declerck,N., Bouillaut,L., Chaix,D., Rugani,N., Slamti,L., Hoh,F., Lereclus,D. and Arold,S.T. (2007) Structure of PlcR: Insights into virulence regulation and evolution of quorum sensing in Gram-positive bacteria. *Proc. Natl. Acad. Sci. U.S.A.*, **104**, 18490–18495.

5. Dunny,G.M. and Berntsson,R.P.-A. (2016) Enterococcal sex pheromones: evolutionary pathways to complex, two-signal systems. *J. Bacteriol.*, **198**, 1556–1562.
6. Neiditch,M.B., Capodagli,G.C., Prehna,G. and Federle,M.J. (2017) Genetic and structural analyses of RRNPP intercellular peptide signaling of Gram-Positive bacteria. *Annu. Rev. Genet.*, **51**, 311–333.
7. Rocha-Estrada,J., Aceves-Diez,A.E., Guarneros,G. and de la Torre,M. (2010) The RNPP family of quorum-sensing proteins in Gram-positive bacteria. *Appl. Microbiol. Biotechnol.*, **87**, 913–923.
8. Dunny,G.M. and Leonard,B.A. (1997) Cell-cell communication in Gram-positive bacteria. *Annu. Rev. Microbiol.*, **51**, 527–564.
9. Bareia,T., Pollak,S. and Eldar,A. (2018) Self-sensing in Bacillus subtilis quorum-sensing systems. *Nat. Microbiol.*, **3**, 83–89.
10. Pottathil,M. and Lazazzera,B.A. (2003) The extracellular Phr peptide-Rap phosphatase signaling circuit of Bacillus subtilis. *Front. Biosci.*, **8**, d32–d45.
11. Gallego del Sol,F. and Marina,A. (2013) Structural basis of Rap phosphatase inhibition by Phr peptides. *PLoS Biol.*, **11**, e1001511.
12. Kohler,V., Keller,W. and Grohmann,E. (2019) Regulation of Gram-positive conjugation. *Front. Microbiol.*, **10**, 1134.
13. Perez-Pascual,D., Monnet,V. and Gardan,R. (2016) Bacterial cell-cell communication in the host via RRNPP peptide-binding regulators. *Front. Microbiol.*, **7**, 706.
14. Gallego Del Sol,F., Penades,J.R. and Marina,A. (2019) Deciphering the molecular mechanism underpinning phage arbitrium communication systems. *Mol. Cell*, **74**, 59–72.
15. Ohara,M., Wu,H.C., Sankaran,K. and Rick,P.D. (1999) Identification and characterization of a new lipoprotein, NlpI, in Escherichia coli K-12. *J. Bacteriol.*, **181**, 4318–4325.
16. Baker,M.D. and Neiditch,M.B. (2011) Structural basis of response regulator inhibition by a bacterial anti-activator protein. *PLoS Biol.*, **9**, e1001226.
17. Parashar,V., Jeffrey,P.D. and Neiditch,M.B. (2013) Conformational change-induced repeat domain expansion regulates Rap phosphatase quorum-sensing signal receptors. *PLoS Biol.*, **11**, e1001512.
18. Parashar,V., Mirouze,N., Dubnau,D.A. and Neiditch,M.B. (2011) Structural basis of response regulator dephosphorylation by Rap phosphatases. *PLoS Biol.*, **9**, e1000589.
19. Do,H. and Kumaraswami,M. (2016) Structural mechanisms of peptide recognition and allosteric modulation of gene regulation by the RRNPP family of quorum-sensing regulators. *J. Mol. Biol.*, **428**, 2793–2804.
20. Perego,M., Hanstein,C., Welsh,K.M., Djavakhishvili,T., Glaser,P. and Hoch,J.A. (1994) Multiple protein-aspartate phosphatases provide a mechanism for the integration of diverse signals in the control of development in B. subtilis. *Cell*, **79**, 1047–1055.
21. Meijer,W.J.J., Wisman,G.B.A., Terpstra,P., Thorsted,P.B., Thomas,C.M., Holsappel,S., Venema,G. and Bron,S. (1998) Rolling-circle plasmids from Bacillus subtilis: complete nucleotide sequences and analyses of genes of pTA1015, pTA1040, pTA1050 and pTA1060, and comparisons with related plasmids from Gram-positive bacteria. *FEMS Microbiol. Rev.*, **21**, 337–368.
22. Singh,P.K., Ramachandran,G., Ramos-Ruiz,R., Peiró-Pastor,R., Abia,D., Wu,L.J. and Meijer,W.J.J. (2013) Mobility of the native Bacillus subtilis conjugative plasmid pLS20 is regulated by intercellular signaling. *PLoS Genet.*, **9**, e1003892.
23. Ramachandran,G., Singh,P.K., Luque-Ortega,J.R., Yuste,L., Alfonso,C., Rojo,F., Wu,L.J. and Meijer,W.J.J. (2014) A complex genetic switch involving overlapping divergent promoters and DNA looping regulates expression of conjugation genes of a gram-positive plasmid. *PLoS Genet.*, **10**, e1004733.
24. Schuster-Böckler,B., Schultz,J. and Rahmann,S. (2004) HMM logos for visualization of protein families. *BMC Bioinformatics*, **5**, 7.
25. Schuck,P. (2000) Size-distribution analysis of macromolecules by sedimentation velocity ultracentrifugation and lamm equation modeling. *Biophys. J.*, **78**, 1606–1619.
26. Laue,T.M., Shah,B.D., Ridgeway,T.M. and Pelletier,S.L. (1992) Computer-Aided Interpretation of analytical sedimentation data for proteins. In: Harding,S.E., Rowe,A.J. and Horton,J.C. (eds). *Analytical Ultracentrifugation in Biochemistry and Polymer Science*. Royal Society of Chemistry, Cambridge, pp. 90–125.
27. Cole,J.L. (2004) Analysis of heterogeneous interactions. *Methods Enzymol.*, **384**, 212–232.

28. Rossi,A.M. and Taylor,C.W. (2011) Analysis of protein-ligand interactions by fluorescence polarization. *Nat. Protoc.*, **6**, 365–387.

29. Petoukhov,M.V., Franke,D., Shkumatov,A.V., Tria,G., Kikhney,A.G., Gajda,M., Gorba,C., Mertens,H.D.T., Konarev,P.V. and Svergun,D.I. (2012) New developments in the ATSAS program package for small-angle scattering data analysis. *J. Appl. Crystallogr.*, **45**, 342–350.

30. Franke,D., Petoukhov,M.V., Konarev,P.V., Panjkovich,A., Tuukkanen,A., Mertens,H.D.T., Kikhney,A.G., Hajizadeh,N.R., Franklin,J.M., Jeffries,C.M. *et al.* (2017) ATSAS 2.8: a comprehensive data analysis suite for small-angle scattering from macromolecular solutions. *J. Appl. Crystallogr.*, **50**, 1212–1225.

31. Svergun,D., Barberato,C. and Koch,M.H.J. (1995) *CRYSOL* – a program to evaluate X-ray solution scattering of biological macromolecules from atomic coordinates. *J. Appl. Crystallogr.*, **28**, 768–773.

32. Konarev,P.V., Volkov,V.V., Sokolova,A.V., Koch,M.H.J. and Svergun,D.I. (2003) PRIMUS: a Windows PC-based system for small-angle scattering data analysis. *J. Appl. Crystallogr.*, **36**, 1277–1282.

33. Juanhuix,J., Gil-Ortiz,F., Cuní,G., Colldelram,C., Nicolás,J., Lidón,J., Boter,E., Ruget,C., Ferrer,S. and Benach,J. (2014) Developments in optics and performance at BL13-XALOC, the macromolecular crystallography beamline at the alba synchrotron. *J. Synchrotron Radiat.*, **21**, 679–689.

34. Vonrhein,C., Flensburg,C., Keller,P., Sharff,A., Smart,O., Paciorek,W., Womack,T. and Bricogne,G. (2011) Data processing and analysis with the *autoPROC* toolbox. *Acta Crystallogr. Sect. D*, **67**, 293–302.

35. Tickle,I.J., Flensburg,C., Keller,P., Paciorek,W., Sharff,A., Vonrhein,C. and Bricogne,G. (2018) STARANISO.

36. McCoy,A.J., Grosse-Kunstleve,R.W., Adams,P.D., Winn,M.D., Storoni,L.C. and Read,R.J. (2007) *Phaser* crystallographic software. *J. Appl. Crystallogr.*, **40**, 658–674.

37. Adams,P.D., Afonine,P.V., Bunkóczi,G., Chen,V.B., Davis,I.W., Echols,N., Headd,J.J., Hung,L.-W., Kapral,G.J., Grosse-Kunstleve,R.W. *et al.* (2010) *PHENIX*: a comprehensive Python-based system for macromolecular structure solution. *Acta Crystallogr. Sect. D*, **66**, 213–221.

38. Emsley,P., Lohkamp,B., Scott,W.G. and Cowtan,K. (2010) Features and Development of Coot. *Acta Crystallogr. D - Biol. Crystallogr.*, **66**, 486.

39. Robert,X. and Gouet,P. (2014) Deciphering key features in protein structures with the new ENDscript server. *Nucleic Acids Res.*, **42**, W320–W324.

40. Berman,H.M., Westbrook,J., Feng,Z., Gilliland,G., Bhat,T.N., Weissig,H., Shindyalov,I.N. and Bourne,P.E. (2000) The Protein Data Bank. *Nucleic Acids Res.*, **28**, 235–242.

41. Krissinel,E. and Henrick,K. (2007) Inference of macromolecular assemblies from crystalline state. *J. Mol. Biol.*, **372**, 774–797.

42. Takayanagi,H., Yuzawa,S. and Sumimoto,H. (2015) Structural basis for the recognition of the scaffold protein Frmpd4/Preso1 by the TPR domain of the adaptor protein LGN. *Acta Crystallogr. F, Struct. Biol. Commun.*, **71**, 175–183.

43. Zhu,J., Wen,W., Zheng,Z., Shang,Y., Wei,Z., Xiao,Z., Pan,Z., Du,Q., Wang,W. and Zhang,M. (2011) LGN/mInsc and LGN/NuMA complex structures suggest distinct functions in asymmetric cell division for the Par3/mInsc/LGN and Gαi/LGN/NuMA pathways. *Mol. Cell*, **43**, 418–431.

44. Rossi,A.M. and Taylor,C.W. (2011) Analysis of protein-ligand interactions by fluorescence polarization. *Nat. Protoc.*, **6**, 365–387.

45. Gesztelyi,R., Zsuga,J., Kemeny-Beke,A., Varga,B., Juhasz,B. and Tosaki,A. (2012) The Hill equation and the origin of quantitative pharmacology. *Arch. Hist. Exact Sci.*, **66**, 427–438.

46. Zouhir,S., Perchat,S., Nicaise,M., Perez,J., Guimaraes,B., Lereclus,D. and Nessler,S. (2013) Peptide-binding dependent conformational changes regulate the transcriptional activity of the quorum-sensor NprR. *Nucleic Acids Res.*, **41**, 7920–7933.

47. Altschul,S.F., Madden,T.L., Schäffer,A.A., Zhang,J., Zhang,Z., Miller,W. and Lipman,D.J. (1997) Gapped BLAST and PSI-BLAST: a new generation of protein database search programs. *Nucleic Acids Res.*, **25**, 3389–3402.

48. Rosch,T.C. and Graumann,P.L. (2015) Induction of plasmid conjugation in bacillus subtilis is bistable and driven by a direct interaction of a Rap/Phr quorum-sensing system with a master repressor. *J. Biol. Chem.*, **290**, 20221–20232.

49. Bae,T. and Dunny,G.M. (2001) Dominant-negative mutants of prgX: evidence for a role for PrgX dimerization in negative regulation of pheromone-inducible conjugation. *Mol. Microbiol.*, **39**, 1307–1320.

50. Kozlowicz,B.K., Shi,K., Gu,Z.-Y., Ohlendorf,D.H., Earhart,C.A. and Dunny,G.M. (2006) Molecular basis for control of conjugation by bacterial pheromone and inhibitor peptides. *Mol. Microbiol.*, **62**, 958–969.

51. Shi,K., Brown,C.K., Gu,Z.-Y., Kozlowicz,B.K., Dunny,G.M., Ohlendorf,D.H. and Earhart,C.A. (2005) Structure of peptide sex pheromone receptor PrgX and PrgX/pheromone complexes and regulation of conjugation in Enterococcus faecalis. *Proc. Natl. Acad. Sci. U.S.A.*, **102**, 18596–18601.